The International Journal of Advanced Manufacturing Technology (2024) 134:3325–3336
https://doi.org/10.1007/s00170-024-14306-z

ORIGINAL ARTICLE

Local and global mechanical properties of orbital friction stir welding on API X65 PSL2 steel / Inconel 625 clad pipes

Carla Volff Amavisca[1,2,3] · Guilherme Vieira Braga Lemos[4,5] · Fabiano Dornelles Ramos[3,6] · Luciano Bergmann[3] · Afonso Reguly[2,5] · Benjamin Klusemann[1,3]

Received: 15 March 2024 / Accepted: 16 August 2024 / Published online: 30 August 2024

Abstract

Orbital friction stir welding (FSW) is a promising approach to joining clad pipes. In this work, the influence of individual process parameters on the material flow even as, mechanical properties in orbital friction stir welded clad pipes is investigated. Due to the local heterogeneous microstructures within the weld, joints were evaluated by optical and scanning electron microscopy (SEM), microhardness, and digital image correlation (DIC). A microhardness increase was observed, with a maximum of 380 $HV_{0.5}$ within the Inconel 625 and 265 $HV_{0.5}$ within the X65 steel stir zones. Sound joints had an average ultimate tensile strength (UTS) exceeding up to 13% of the calculated theoretical tensile strength, which is obtained considering the minimum tensile strength of both materials. Additionally, failure occurred in the base material during the tensile testing, where the local strain in the stir zones of the X65 steel and Inconel 625 were only 3.3% and 10%, respectively. In summary, this investigation shows friction stir welded joints of API X65 steel and Inconel 625 clad pipes with high mechanical properties.

Keywords Orbital friction stir welding · Cladded pipe · X65 steel · Inconel 625 · Microstructure, Mechanical properties

1 Introduction

Joining dissimilar high-melting point materials such as high-strength steel and nickel-based alloys usually leads to major challenges due to the limited solubility of the elements, which may result in the formation of brittle intermetallic compounds (IMC) [1]. However, this dissimilar combination is widely used in the oil and gas and chemical industries, due to its high mechanical properties and corrosion resistance [2]. These pipes are based on steel pipes with an internal corrosion-resistant alloy (CRA) cladding, which protects the carbon steel against hydrogen embrittlement, and sulfide stress corrosion cracking, amongst others [3].

Conventional fusion-based welding processes are typically used for joining clad pipes [2–5], where the materials undergo melting followed by solidification, which can lead to degradation of material properties and increase susceptibility to hot cracking [5, 6]. Friction Stir Welding (FSW) [7], on the other hand, is a solid-state joining process [8–13]. It uses the mechanical friction energy produced between the materials to be joined by moving a non-consumable rotating tool, along the joint interface. While the tool translates, the velocity difference between

✉ Carla Volff Amavisca
carla.amavisca@stud.leuphana.de

1 Institute for Production Technology and Systems, Leuphana University Lüneburg, Universitätsallee 1, 21335 Lüneburg, Germany

2 Federal University of Rio Grande Do Sul (UFRGS), Av. Osvaldo Aranha 99 S.610, Porto Alegre 90035-190, Brazil

3 Institute of Materials Mechanics, Solid-State Materials Processing, Helmholtz-Zentrum Hereon, Max-Plank-Straße 1, 21502 Geesthacht, Germany

4 Federal University of Santa Maria (UFSM), Rod. Taufik Germano, 3013, Cachoeira Do Sul 96503-205, Brazil

5 Physical Metallurgy Laboratory (LAMEF) - PPGE3M/UFRGS, Av. Osvaldo Aranha 99 S.610, Porto Alegre 90035-190, Brazil

6 Federal Institute of Rio Grande Do Sul (IFRS), R. Avelino Antônio de Souza 1730, Caxias Do Sul 95043-700, Brazil

Table 1 Chemical composition of the steel X65 and Inconel 625 layers (%wt.) [28]

Element	Ni	Cr	Mo	Fe	Si	Mn	C	Al	P	S
API X65 PSL2	0.15	0.16	-	Bal	0.32	1.58	0.05	0.04	0.01	0.002
Inconel 625	58.19	22.09	7.51	4.46	-	0.37	-	1.18	-	-

the rotating tool and the work material surface creates friction work and subsequently, heat [8]. The heat generated by friction and severe plastic deformation (SPD) softens the material, reduces its strength and the flow of the plasticized material occurs. The plasticized material is transported from the front of the tool to the back, where it is forged, producing the joint. Due to the SPD, the weld joints result in refined and equiaxed recrystallized grains associated with good mechanical properties [8, 14–18]. Due to its advantages, such as high process flexibility, precise external control, ability to weld dissimilar materials, and high levels of repeatability [9, 12, 19], the FSW process has been developed [20, 21], and it has been increasingly used in the industry [22].

Studies on FSW for joining dissimilar materials such as carbon steels and Ni-based alloys are limited and this area remains to be explored. Song et al. [23] studied the microstructural and mechanical properties of dissimilar joints, where the FSW reduced the grain size of Inconel 600 from 20 µm in the base material to 8.5 µm in the stir zone. Rodriguez and Ramirez [24] investigated the FSW process parameters to weld 6 mm thick dissimilar butt joints of mild steel and Ni-based alloy 625. The resulting welds showed a complex microstructure, leading to the differentiation into six different microstructure zones and the interface region consisted of deformed and recrystallized fcc grains with NbC carbides. Lessa et al. [25] and Landell et al. [26] analyzed the effectiveness of two-pass FSW on steel sheets clad with Inconel 625. Joints without defects were produced with notable grain refinement in the stir zone and improved mechanical properties. In a recent study, Bossle et al. [27] welded by FSW dissimilar lap sheets of GL E38 steel and Inconel 625. The joint interface showed the formation of a typical hook from Inconel 625 but no IMC were found via SEM. Finally, the orbital FSW of clad pipes (API X65 and Inconel 625) was analyzed by Amavisca et al. [28] where defect-free welds in one pass and full tool penetration were obtained.

The study made by Amavisca et al. [28] has focused on the feasibility of orbital FSW for clad pipes, along with the development of a rigid clamping system for joining these pipes. The present work aims to investigate joints produced by different orbital FSW parameters and subsequently, test them through tensile tests and compare their local–global deformation mechanisms. For this approach, digital image correlation (DIC), and microstructural and fracture analysis were employed.

2 Experimental procedure

2.1 Material selection and process parameters

The clad pipes used in this study were provided by Butting GmbH & Co, with an outer diameter of 310.5 mm and a wall thickness of 9 mm. The pipes, composed of API X65 PSL2 steel (6 mm thick) and Inconel 625 (3 mm thick), were metallurgically bonded by a hot roll-bonding process. The base material chemical composition was determined via optical emission spectrometry and energy dispersive spectroscopy (EDS) for the X65 steel and Inconel 625, respectively, see Table 1.

Single-pass orbital FSW was performed on the butt sections of the clad pipes. The tool tilt angle was 0.5°, and argon as shielding gas was employed to protect the weld surface from oxidation.[1] Based on previous studies [25, 26], the process parameters were chosen to build a matrix of parameters with three different input factors, i.e., axial force, rotational speed, and welding speed. Two levels of each process parameter were investigated, resulting in eight welded joints, see Table 2. The calculated energy input is based on the parameters and measured machine torque during the orbital FSW processes.

The FSW tool used was a MegaStir™ polycrystalline cubic boron nitride (pcBN) tool, designated as Q70, i.e., 70 wt. % pcBN and 30 wt. % W–Re binder material. The tool has a convex radius shoulder with a diameter of 25 mm and a stepped spiral probe with a length of 8.5 mm. A pipe manipulator with internal clamp, external rollers, and lateral clamping was designed to guarantee proper clamping of the pipes. For more details about the clamping system, the interested reader is referred to Amavisca et al. [28].

2.2 Macrostructure and mechanical characterization

The macro and microstructures, including a small fraction of secondary constituents, were analyzed by optical microscopy (OM) and scanning electron microscopy (SEM) equipped with the EDAX Apollo X EDS system. The samples were prepared using a standard metallographic procedure followed by a two-step etching: First, Nital 2%-vol was used to

[1] Please note that in our previous study [28], a tool tilt angle of 0.0° was used.

Table 2 Performed orbital welding experiments at different process parameters, including calculated energy input during welding and revolutionary pitch

Weld	Force (kN)	Rotational Speed (rpm)	Welding Speed (mm/s)	Energy Input[2] (kJ/mm)	Revolutionary Pitch (mm/rev)
I	45	400	2	2.14	0.30
II	45	400	3	1.60	0.45
III	45	500	2	2.25	0.24
IV	45	500	3	1.75	0.36
V	50	400	2	2.29	0.30
VI	50	400	3	-[3]	0.45
VII	50	500	2	3.20	0.24
VIII	50	500	3	1.85	0.36

[2] $EI = \frac{w\tau}{v}$, were w is the rotational speed (in rad/s), τ is the torque and v is the welding speed

[3] Tool probe broke during the weld plunge stage

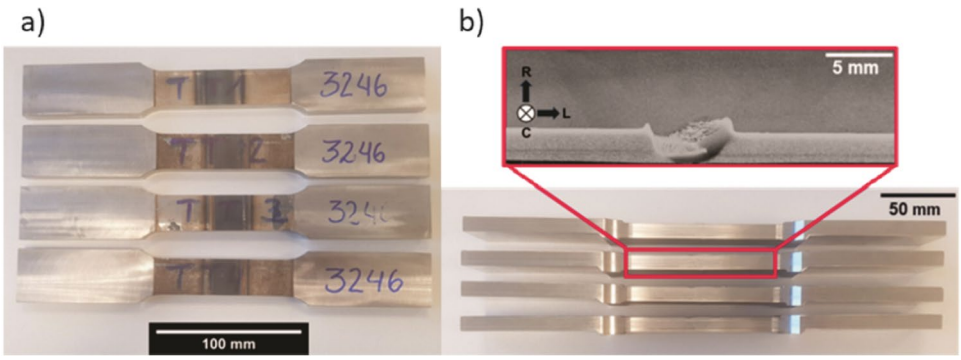

Fig. 1 **a** Weld tensile samples with the full thickness of the pipe; **b** region where DIC analysis was carried out

reveal the steel microstructure, then Adler's solution (25 ml H_2O, 3 g $CuCl_2$, 15 g $FeCl_3$, 50 ml HCl) used to reveal the Inconel 625 microstructure.

Vickers microhardness tests were performed using a 500 gf load (HV0.5) and 0.5 mm distance between indentations. Uniaxial tensile tests were based on ISO 4136:2022(E) standard [29], using a Zwick/Roell universal testing machine with a load capacity of 200 kN. Four samples of each parameter were tested at room temperature (RT) and constant crosshead speed of 1 mm/min. The displacement was recorded via an MTS extensometer (gauge length of 75 mm). The weld region was tested "as produced", i.e., the weld region was not machined or gridded before the test. The dimensions of the tensile test samples are shown in Fig. 1a.

According to the API 5L specification [30], the minimum elongation (Af) shall be calculated according to Eq. 1:

$$Af = C\frac{A_{Xc}^{0.2}}{U^{0.9}} \tag{1}$$

where C is 1940, A_{XC} is the cross-sectional area of the tensile specimen, and U is the minimum tensile strength.

From the standards API SPEC 5L [30], the orbital weld shall, at least, reach the minimum mechanical strength of the BM_{X65}. For the mechanical tests, the corrosion-resistant alloy (CRA) layer shall be removed, however, for research purposes and understanding of the welded interface, altered by FSW, the clad layer was not removed in this study.

In this case, the standard DNVGL-RU-SHIPS Pt.2Ch.2:2018 [31], with requirements for metallic materials used for manufacturing vessels and related equipment, shows an alternative for calculating the minimum tensile strength. Accordingly, the equation considers the mechanical properties of both materials. The tensile strength shall be higher than the theoretical value calculated by Eq. 2:

$$R_m = \frac{S_1 * R_{m1} + S_2 * R_{m2}}{S} \tag{2}$$

R_{m1} is the substrate minimum tensile strength, R_{m2} is the clad minimum tensile strength, S is the pipe thickness, S_1 is the substrate thickness, and S_2 is the clad layer thickness. In this study, S = 9 mm, S_1 = 6 mm, S_2 = 3 mm, and R_{m1} and R_{m2} were considered 535 MPa [30] and 690 MPa [32], respectively. According to Eq. 2, the theoretical tensile strength for the base material (BM[2]) is 586.7 MPa.

[2] BM refers to the base material as received (X65 steel and Inconel 625).

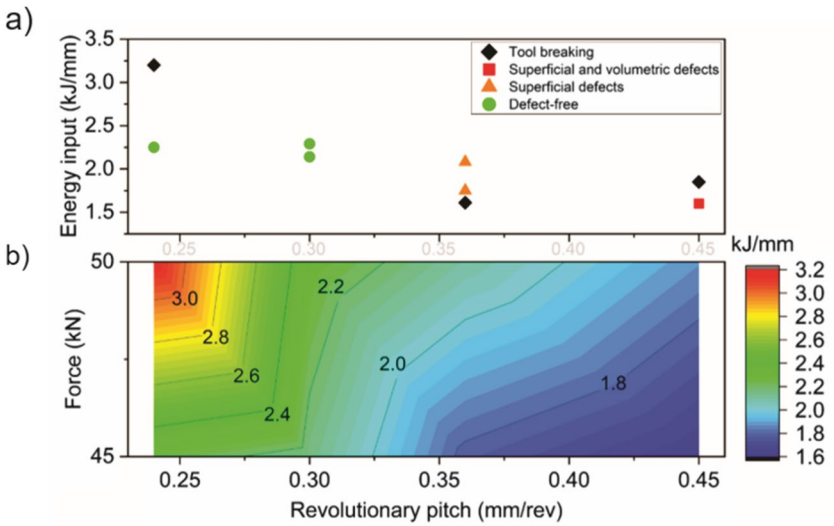

Fig. 2 **a** Successful and faulty process parameters correlated to energy input vs revolutionary pitch of an API X65 PSL 2 and Inconel 625 clad pipe welded by orbital friction stir welding; **b** Axial force vs revolutionary pitch for different energy inputs

A GOM digital image correlation (DIC) system linked to the tensile test machine was used for assessing the local strain behavior in the cross-section of the transverse tensile samples, see Fig. 1b. Speckled patterns of the specimen surface were analyzed before and after deformation, which was used to track the movement of the marked points on the specimen surface to calculate the local–global strain distribution. The measurements, evaluations, and documentation were accomplished with the ARAMIS software.

3 Results and discussion

3.1 Welding process

During the development of suitable process parameters on clad pipes, eight welds were produced to evaluate the individual process parameters and then maximize joint mechanical properties and minimize energy consumption. In Fig. 2a, the variation on the revolutionary pitch (RP) process parameter, i.e., the ratio between the welding speed and rotation speed, and the energy input (EI) are correlated, where a set of successful and faulty process parameters can be identified. Defect-free welds were seen in a small window of RP, ranging between 0.24 – 0.30 mm/rev and EI between 2.14 – 2.29 kJ/mm. The axial forces, i.e., 45 and 50 kN, are correlated to the RP, as well, to identify their contribution to the EI, see Fig. 2b. These results are in agreement with Lessa et al. [25], who affirmed that low-energy input, i.e., under 2.30 kJ/mm, is important for producing sound joints, in particular to Inconel 625.

3.2 Macro and microstructural observations

Macrostructures of orbital friction stir welded clad pipes are shown in Fig. 3. Three characteristic regions can be distinguished: the API X65 PSL 2 steel side (upper part), the Inconel 625 side (bottom part), and the tool probe zone, where the mixing of dissimilar alloys occurred. The regions in the steel include the heat-affected zone (HAZ_{X65}), the stir zone (SZ_{X65}), and the hard zone (HZ_{X65}), which is reported as the zone that experiences the highest temperature and strain rates at the top of the AS [33–35]. The BM_{X65} was composed of mainly acicular ferrite (AF), whereas the HAZ_{X65} consists of quasi-polygonal ferrite (QPF), polygonal ferrite (PF), and AF. The SZ_{X65} has a microstructure of AF, and granular bainite (GB), and the HZ_{X65} is composed of GB and lath bainite (LB). Moreover, a small fraction of the martensite-austenite phase (M/A) was also found in the SZ_{X65}, which agrees with the observations from Mohammadjoo et al. [36] and Buzzatti et al. [37].

In the Ni-based alloy, the BM_{625} of elongated austenitic grains was transformed in the thermo-mechanically affected zone ($TMAZ_{625}$) and the stir zone (SZ_{625}). The FSW process led to significant grain refinement in the bottom of SZ_{625}, which can be attributed to dynamic recrystallization (DRX). The $TMAZ_{625}$ presented a deformed microstructure with many sub-grains following the probe flow pattern. Moreover, hooks of Inconel 625 on the advancing (AS) and retreating side (RS) can be identified. The microstructure in the hooks presented coarser and recrystallized austenitic grains, which suggests that the material was exposed to higher thermal cycles compared to the SZ_{625}, causing grain growth. For details on the resulting microstructural characteristics of orbital FSW on API X65 PSL2 and Inconel 625 clad pipes, the interested reader is referred to Amavisca et al. [28].

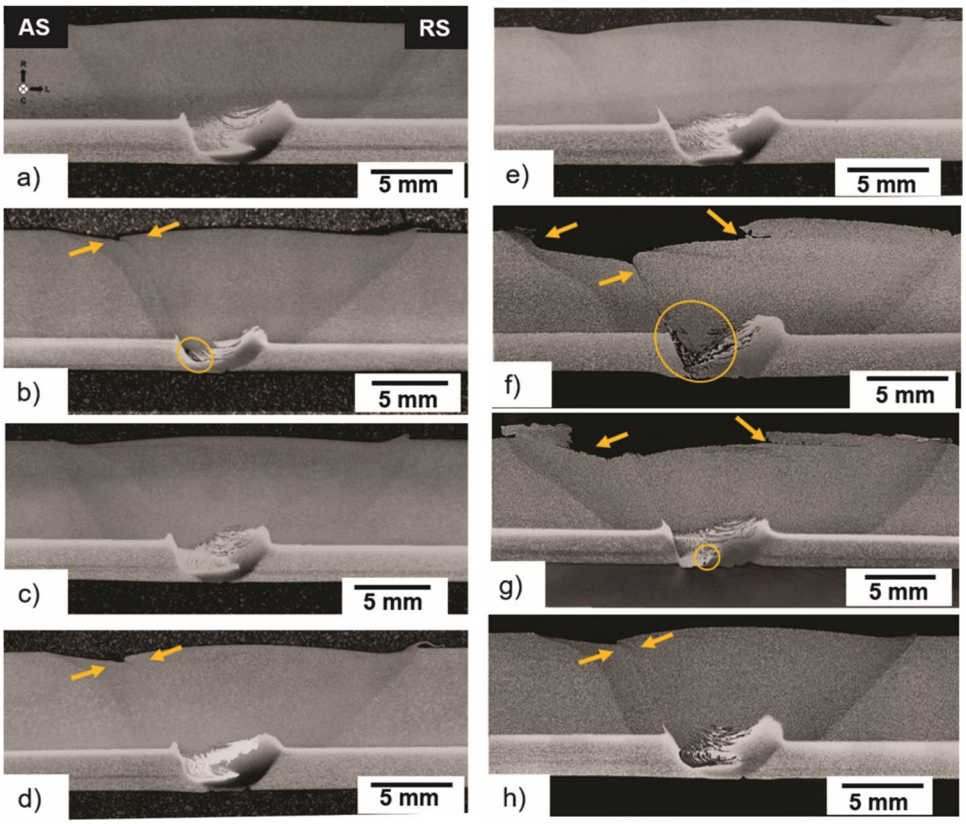

Fig. 3 Macrostructures of FSW joints of clad pipes under different process parameters; **a** Weld I; **b** Weld II; **c** Weld III; **d** Weld IV and **e** Weld V; **f** Weld VI; **g** Weld VII and **h** Weld VIII. In all Figures, the AS is on the left side, and the RS is on the right side, according to Fig. 3a)

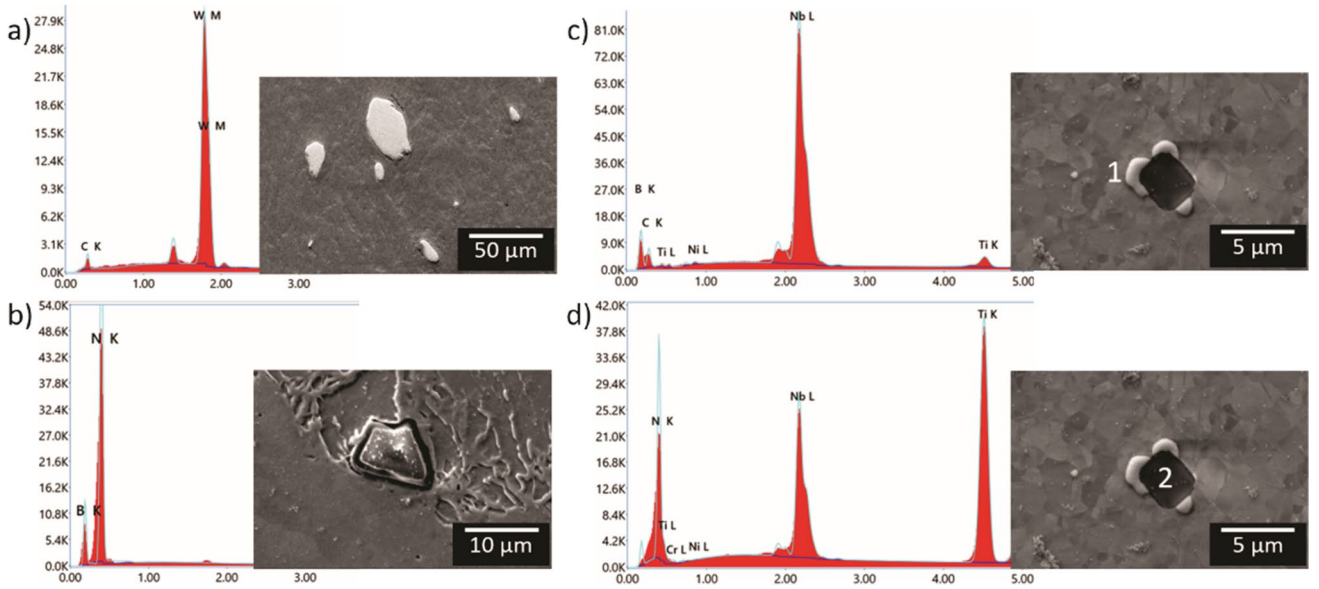

Fig. 4 SEM images and EDS analysis of particles found in different welds: **a** flash of Weld VII, **b** SZ_{X65} of Weld VIII, and **c**-**d** SZ_{625} of Weld III

Welds I, III, and V, Fig. 3a, c, e, produced with energy input ≥ 2.14 kJ/mm but ≤ 2.29 kJ/mm, showed good top surface quality and no volumetric defects. In contrast, joints with EI ≤ 1.85 kJ/mm resulted in welds with void and or superficial defects at the AS of the SZ_{625}, or even more, tool breakage, suggesting low energy generation and insufficient plasticizing of the materials during the FSW process [38]. According to Bagheri et al. [39] and Abdollahzadeh et al. [40], the low solubility and thermal stress between dissimilar materials may cause voids. On the other hand, the joint

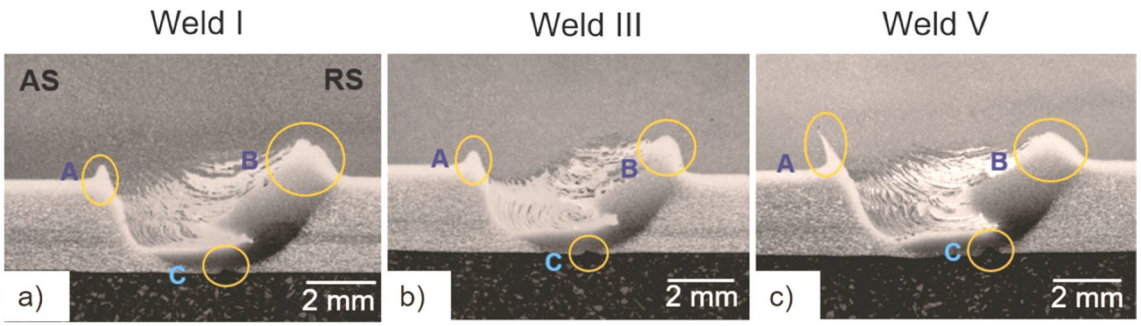

Fig. 5 Joint interface formation of welds a) I, b) III, c) V. Three characteristics are highlighted: hook on the AS (**A**), hook on the RS (**B**), and lack of bonding on the weld root (**C**)

Table 3 Welded joint characteristics, see Fig. 5, where (A) is the size of the hook on the AS, (B) is the size of the hook on the RS, and (C) characterizes the lack of bonding on the weld root

Weld	A (mm)	B (mm)	C (mm)
I	0.43	1.31	0.18
III	0.41	1.19	0.15
V	1.63	0.82	0.22

Table 4 Process parameters influence the size of the joint characteristics: (A) the size of the hook on the AS; (B) the size of the hook on the RS and (C) the lack of bonding on the weld root

Process Parameters	A	B	C
↑ Axial force (kN)	↑	↓	↑
↑ Rotational speed (rpm)	↑	↑	↓

produced with EI > 3.0 kJ/mm also resulted in a tool breakage, Fig. 3g. According to studies [41–43], pcBN tool wear can be caused by detachment of BN grains due to thermal softening of the W–Re binder phase and dissolution of BN in the hot material in the stirred zone. Tungsten, nitrogen, and boron content were identified in Weld VII and Weld VIII via EDS analysis Fig. 4a–b, respectively.

In terms of Inconel 625, in all zones of the weld joint, carbonitrides inherent to the BM_{625} were observed along the grain boundaries and in the grain interiors with various morphologies and sizes, such as (Nb) C, (Nb, Ti) N, Fig. 4c-d. Mani et al. [44] via thermodynamic simulation of joint welding solidification of API 5L X65 steel and Ni-based alloys, reported that the increase in dilution promoted a tendency for the nucleation of the M_6C phases and complex carbides to become stable. The simulation also predicted secondary phases, such as Laves, Ni_3Nb, Ni_3Ti, σ, and η phase, for the alloys containing Nb and Ti. In the FSW welding joints, however, via SEM investigation, no microstructural evidence of precipitate transformation during the thermal cycle was observed, only a change in size, probably due to the SPD that may have broken some carbonitrides. According to Lippold et al. [1] and David et al. [45], the precipitates in the alloy 625, after long heat treatment times, or depending on the thermomechanical process route, can be transformed into brittle phases.

In the following, only sound welds were further analyzed, i.e., welds I, III, and V. The formation of the alternate layers of X65 steel and Inconel 625 is attributed to the thermal softening and plastic flow of both materials, it occurred due to the shearing of Inconel 625 beneath the tool probe [27]. The results in Fig. 5 show clear evidence of the differences in the material mixing due to the different welding parameters, characterized by the height of the hook on the AS (A), the hook on the RS (B), and the lack of bonding on the weld root (C), see Table 3.

According to Ferreira et al. [12], defects such as a lack of bonding on the root weld, are not directly related to the process parameters but instead are likely to improper conditions in the system or apparatus. However, the current results show clear evidence of differences in the lack of bonding on the root weld (C) owing to the welding parameters employed, see Table 4, where the lack of bonding (C) can be reduced by increasing the tool rotational speed and decreasing the axial force and as well the height of the hooks in the AS and RS, (A) and (B), respectively are influenced by the process parameters.

3.3 Microhardness test

Microhardness tests of the base material led to an average of 210 $HV_{0.5}$, 249 $HV_{0.5}$, and 318 $HV_{0.5}$ for the BM_{X65}, hot roll-bonding interface, and the BM_{625}, respectively. Figures 6a-c depict the hardness maps in the Welds I, III, and V along the cross-section, respectively. The hardness values slightly increased in the SZ_{X65} (215 $HV_{0.5}$), which is expected due to the severe plastic deformation at elevated temperatures and high cooling rate, resulting in a bainite microstructure [34]. On the AS and top surface, the HZ_{X65} presents a higher hardness (250 $HV_{0.5}$) associated with high concentrations of lath bainite. Equiaxial PF grains found at the HAZ $_{X65}$

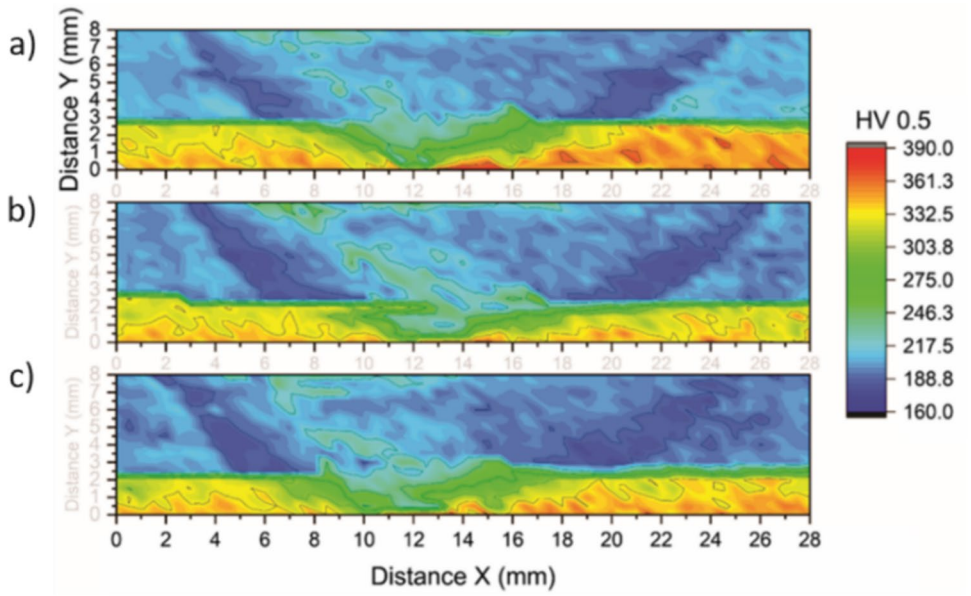

Fig. 6 Microhardness map of welds: a) I, b) III, and c) V. In all Figures, the AS is on the left side, and the RS is on the right side, according to Fig. 3a

resulted in a lower microhardness zone (around 180 $HV_{0.5}$) on both sides, which agrees with the results in the literature [46, 47]. All the sound welds in this study have very similar energy input, and the microstructure and, consequently, the hardness are very similar.

In terms of Inconel 625, all welds showed a peak of hardness (~380 $HV_{0.5}$) near the bottom weld center, which can be attributed to the activation of the recovery and recrystallization mechanisms during FSW that led to grain refinement of the microstructure. In the hooks at the AS and RS, relatively coarse recrystallized Inconel 625 grains were found, and according to the Hall–Petch equation,[3] the hardness drops to 280 $HV_{0.5}$. In the $TMAZ_{625}$ region, the hardness maximum values were 330 $HV_{0.5}$. The lowest hardness (215 $HV_{0.5}$) was found in the mixture region, due to the greater amount of Fe in the lamellar layer [48, 49]. According to Murr et al. [49], these complex intercalation patterns alter the microstructural spacing and structure, which account for the hardness variations. As more steel is introduced in the Inconel microstructure, the microstructure on the Inconel side gets softer. Moreover, the mixture of materials seems more likely to be in welds with higher energy input.

3.4 Tensile test

Figure 7 summarizes the resulting average ultimate tensile strength (UTS), yield strength[4] (YS), and fracture elongation for the steel BM and welded joints, determined through tensile testing. The BM_{X65} shows an average UTS of 553 ± 5 MPa, YS of 524 ± 3 MPa, and elongation of 23.9%, which is consistent with the API SPEC 5L standard [30], where the UTS and YS range for the API X65 PSL 2 from 535 MPa—760 MPa and 450 MPa – 600 MPa, respectively. The minimum elongation, according to Eq. 1, is around 17.5%. For Inconel 625, according to the ASTM B705-17 standard [32], the UTS and YS are reported as 690 MPa and 276 MPa, respectively. All welds I, III, and V met the API SPEC 5L standard requirement [30] for the UTS, YS, and the theoretical tensile strength (586.7 MPa) calculated by Eq. 2. An improvement in the mechanical properties is expected in the SZ for both materials, due to grain refinement in the Inconel SZ_{625} [50, 51] and the allotropic transformation in the SZ_{X65} [52, 53]. In contrast,

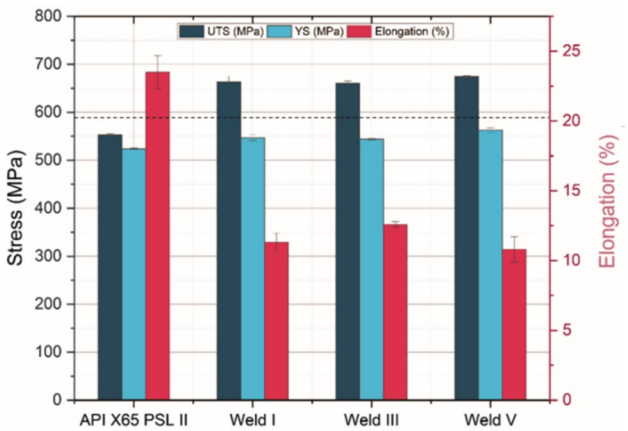

Fig. 7 Tensile test results for the BM of steel API X65 and Welds I (45 kN, 400 rpm, 2 mm/s), III (45 kN, 500 rpm, 2 mm/s) and V (50 kN, 400 rpm, 2 mm/s). The dashed line indicates the theoretical tensile strength

[3] $\Delta\sigma = \frac{K_y}{\sqrt{d}}$, where $\Delta\sigma$ is the yield strength, K_y is the strengthening coefficient of the material, and d is the average grain diameter.

[4] YS is determined with the 0.2% offset method from the stress–strain curves.

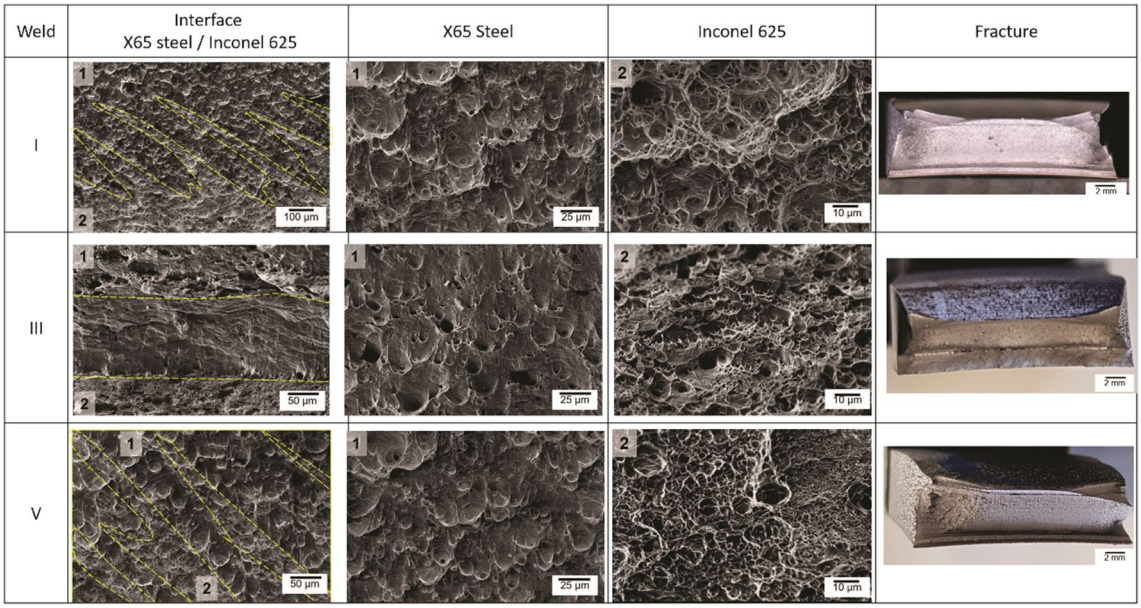

Fig. 8 SEM fractography analysis of the welds I, III, and V in the interface, Inconel 625 side and steel X65 side. Numbers 1 and 2 indicate the steel and Inconel sides, respectively

the elongation of the joints is significantly lower than that of the BM_{X65}, which can be attributed to the highly mixed microstructure (HAZ, TMAZ, SZ, and HZ) throughout the joint, resulting in a heterogeneous deformation during the tensile testing. This mixed microstructure results from an asymmetric material flow, SPD, and thermal cycle during the FSW process [54]. Different local strains typically lead to lower elongation, i.e., earlier fracture compared to materials deforming more homogeneous, such as the received BM [55].

All welds presented high tensile strength and yield strength, however, the tensile specimens failed within the weld zone, except Weld III. One possible explanation for this is a detected lack of bonding in the weld root named (C), observed in all welds, see Fig. 5, that might act as stress concentration, leading to failure within the SZ_{625}. Such a defect was expected in the current experiment, as a small space between the pipe wall and the tool height was needed to avoid touching between the tool and the internal clamping that could cause the breakage of the tool or the joining of the pipes to the internal clamping. The lack of bonding in the weld root (C) was measured, see Table 3, and it was observed that only the welded joint with the lowest value of (C) had all the failures in the BM, i.e., when (C) was ≤ 15 mm, it did not influence in the tensile tests and the failures occurred in the BM.

3.5 Fractography analysis

Figure 8 shows the fracture surface morphology of joints under different welding conditions. The location of the failure of the tensile test samples was found at the SZ_{X65}/HAZ_{X65}, for Welds I and V and at the base material for Weld III. All joints indicate ductile fracture mechanisms,

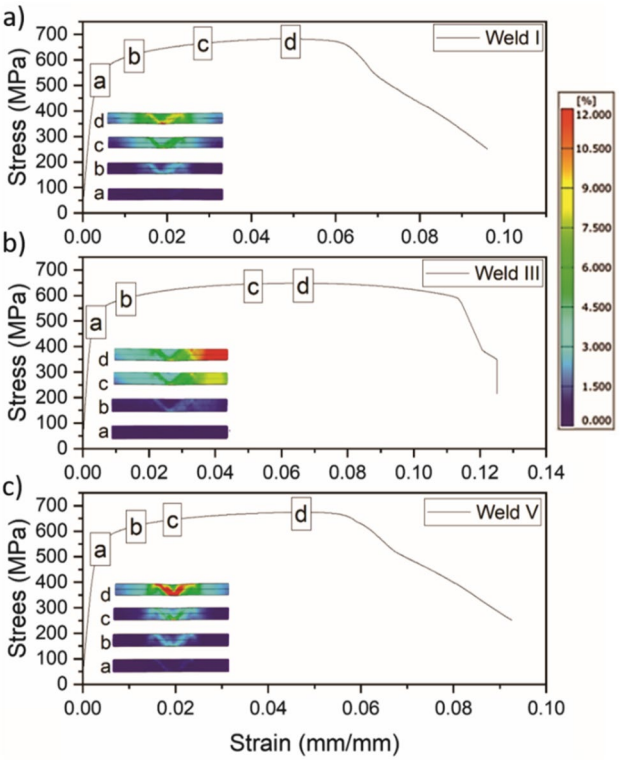

Fig. 9 **a**-**c** Stress–strain curves and DIC maps for one sample of each weld: a) Weld I, b) Weld III, and c) Weld V. Characteristic marked points in the curve represent a) YS and d) UTS

including dimples and voids of different sizes [56]. The presence of two distinct phases with different mechanical properties leads to discrepancy in elongation and accordingly results in variation in fracture mode [57]. The lack of bonding in the welding bottom also acted as a stress concentration and fracture initiation point and may be the reason for the fractures in Welds I and V.

3.6 Digital image correlation

The DIC technique was employed to investigate the evolution of the strains in the welded joints at different global strains. Figure 9 shows the stress–strain curves with distinct frames of deformation for the three welds before fracture. With ongoing tensile tests, the local strain varies for the three welds. These local strain variations can be attributed to the asymmetric material flow, SPD, and thermal cycle, which took place during the FSW process [55].

The tensile test specimens in the cross-section cover different microstructures, i.e., BM, HZ_{X65}, HAZ_{X65}, $TMAZ_{625}$, SZ_{X65}, and SZ_{625}. The distinct zones have different resistances to deformation due to the distinct microstructures present. For welds I and V, the first local strain peak, around 3%, was observed in the SZ_{X65}/HAZ_{X65}, Fig. 9a and c. The SZ_{X65}/HAZ_{X65} undergoes the highest strain, and during tension, the lack of bonding on the weld root grows fast until fracture the joint in the SZ_{625}/HAZ_{X65} region. For Weld III, however, initially, the local strain was very similar in the SZ_{X65}/HAZ_{X65} and BM, but with increasing global strain, the local strain distribution shifted to the BM eventually resulting in necking and fracture within the BM, Fig. 9b.

Regarding Weld III, Fig. 10a shows the local strain profile along a line on the X65 steel side and Fig. 10b on the Inconel 625 side at different global strains. Until YS is reached, the sample deforms nearly uniformly. But with ongoing deformation, the strain inhomogeneity increases.

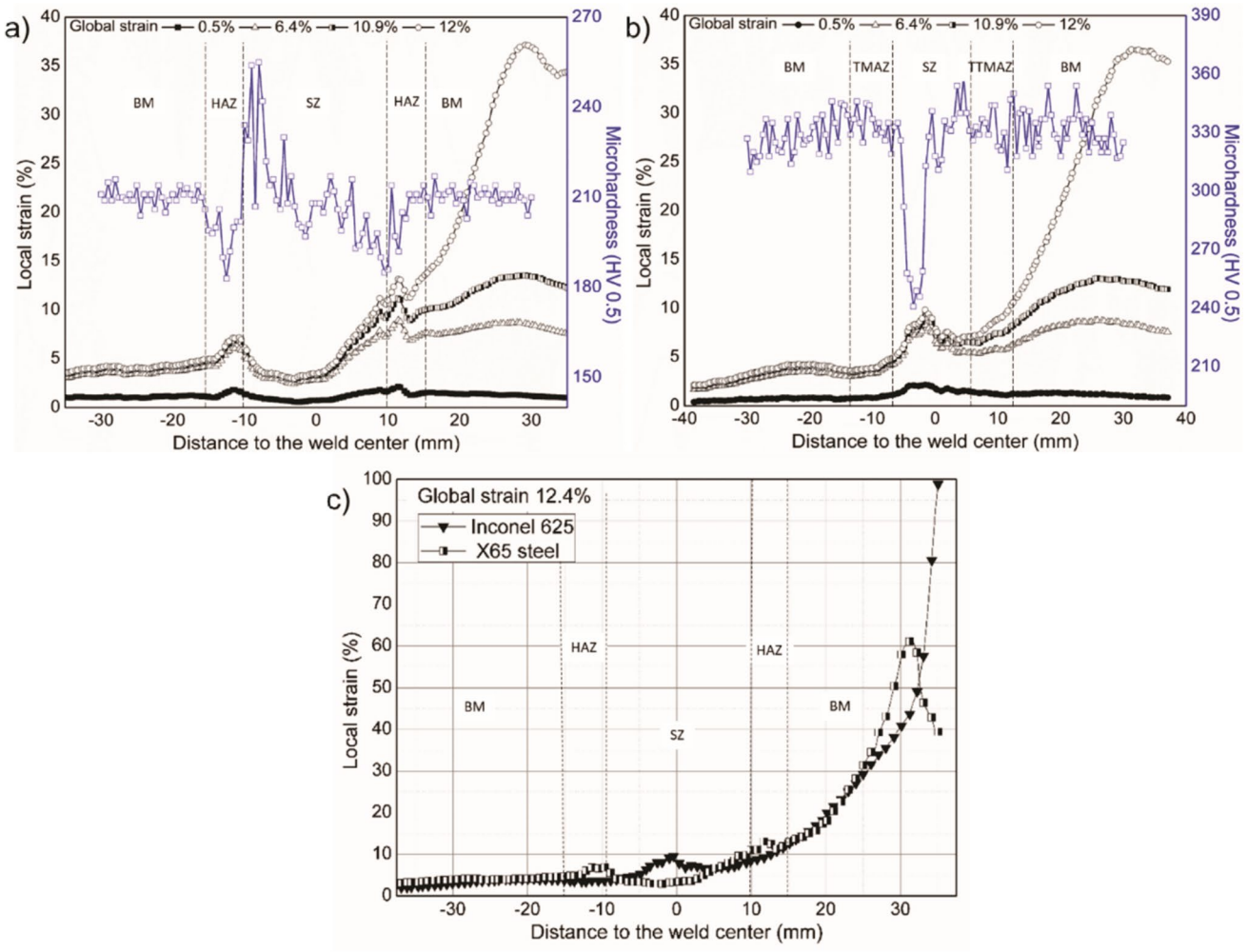

Fig. 10 Local strain of Weld III during tensile test along a profile line under different global strains and hardness profile: **a** X65 steel side, **b** Inconel 625 side, **c** local strain in the weld zones at the failure

For instance, at 6.4% global strain, the highest local strains are located in the HAZ_{X65} (11.5%) and BM_{X65} (13.8%), representing nearly two times the global strain. In contrast, in the SZ_{X65} the local strain is about 3%. On the Inconel side, the highest local strains are found in the SZ_{625} and BM_{625} with 9.3% and 13%, respectively. At 12% global strain, the highest local strain has already increased in the BM of both materials to 35%. Shortly before fracture at a global strain of 12.4%, Fig. 9c, the local strain of the BM_{625} reached a value over 100%. At the fracture moment, the local strains in the SZ_{X65} and SZ_{625} are only 3.3% and 10%, respectively.

Due to differences in grain size and microstructural transformation, the microstructural zones show different mechanical properties, and therefore resistance to deformation. For example, acicular ferrite consists of thin, lenticular plates; its small grain size and high density of high-angle grain boundaries inhibit cleavage propagation and can increase toughness and strength; polygonal ferrite increases the ductility of steels, but if the grain size is coarse, it can result in lower strengths; bainitic microstructures contain a high density of dislocations that result in higher strength and lower ductility [58]. Analyzing the hardness distribution along the joint, the HAZ_{X65}, BM, and SZ_{625} exhibit the lowest hardness, therefore, in these locations, the strain is higher during loading. The hot roll-bonding interface gradually becomes the deformation weak area and finally, the fracture occurs in this region.

4 Conclusions

Orbital friction stir welding (FSW) has been successfully employed in clad pipes of API X65 steel and Inconel 625. The current outcomes can be summarized as follows:

- A process parameters window of defect-free welds was identified at a revolutionary pitch of 0.24 – 0.30 mm/rev and energy input ranging from 2.14 to 2.29 kJ/mm. Typical hooks of Inconel 625 were formed at the stir zone (SZ) interface on the advancing side (AS) and retreating side (RS), and their sizes varied with the process parameters.
- No microstructural evidence of secondary phases, such as Laves, Ni3Nb, Ni_3Ti, σ, and η phases were observed via SEM analysis.
- Defect-free welds (I, III, and V) showed a tensile strength of 663 MPa, 660 MPa, and 674 MPa, respectively. The result exceeded 11.5%, 11.1%, and 13%, respectively of the minimum calculated theoretical tensile strength, however, only Weld III failed within the BM. The lack of bonding on the weld root (C) (also seen in all the welds) affected the mechanical properties, acting as a stress concentration area during tensile testing.
- Due to the local microstructural changes produced by FSW, the local strain throughout the welded joint is heterogeneous and is inversely proportional to the local hardness. For Weld III, when the BM_{625} experienced locally 100% strain during tensile testing, the local strains in the SZ_{X65} and SZ_{625} were only 3.3% and 10%, respectively.

Acknowledgements This work was conducted during a scholarship supported by Leuphana University Lüneburg (Carla Volff Amavisca), which is gratefully acknowledged. Financial support from DAAD via funds of the Federal Ministry of Education and Research (BMBF) under project number 57598245 is gratefully acknowledged. Financed by Capes – Brazilian Federal Agency for Support and Evaluation of Graduate Education within the Ministry of Education of Brazil (Fabiano Dornelles Ramos) is gratefully acknowledged.

Author contributions C.V.A.: conceptualization, methodology, data curation, investigation, formal analysis, writing, and editing; G.V.B.L.: investigation, writing, review, and editing; F.D.R.: friction stir welding, investigation and review; L.B.: friction stir welding, investigation and review; A.R.: supervision and review; B.K: conceptualization, supervision, writing, review, and editing.

Funding Open Access funding enabled and organized by Projekt DEAL. This publication was funded by the German Research Foundation (DFG).

Data availability The datasets used and/or analyzed during the current study are available from the corresponding author upon reasonable request.

Declarations

Competing interests The authors declare no competing interests.

References

1. Lippold JC, Kiser SD, DuPont JN (2011) Welding metallurgy and weldability of nickel-base alloys. John Wiley & Sons
2. Reichel T et al (2008) Production of Metallurgically Cladded Pipes for High End Applications in the Oil and Gas Industry. International Conference on Offshore Mechanics and Artic Engineering, 2008, Estoril, Portugal. v. 5: Materials Technology; CFD

and VIV. Estoril, Portugal: ASMEDC, p 179–186. https://doi.org/10.1115/OMAE2008-57311
3. Bunaziv, Olden V, Akselsen OM (2019) Metallurgical Aspects in the Welding of Clad Pipelines—A Global Outlook. Appl Sci 9(15):3118. https://doi.org/10.3390/app9153118
4. Giudice F et al (2020) Metallurgical Characterization of the Interfaces in Steel Plates Clad with Austenitic Steel or High Ni Alloys by Hot Rolling. Metals 10(2):286. https://doi.org/10.3390/met10020286
5. Xu LY, Jing HY, Han YD (2018) Effect of welding on the corrosion behavior of X65/Inconel 625 in simulated solution. Weld. World 62:363–375. https://doi.org/10.1007/s40194-018-0549-y
6. DuPont JN (1996) Solidification of an alloy 625 weld overlay. Metall Mater Trans A 27:3612–3620. https://doi.org/10.1007/BF02595452
7. Thomas WM, Nicholas ED, Needham JC, Murch MG, Temple-Smith P, Dawes CJ (1991) Improvements relating to friction welding. Patent No. 5,460,317
8. Tahir J, Abdullah J, Hussain Z, Putra I (2012) Principles and Thermo-Mechanical Model of Friction Stir Welding. Welding Processes. InTech. https://doi.org/10.5772/50156
9. Gibson BT et al (2014) Friction stir welding: Process, automation, and control. J Manuf Process 16(1):56–73. https://doi.org/10.1016/j.jmapro.2013.04.002
10. Mishra RS, Ma ZY (2005) Friction stir welding and processing. Mater Sci Eng R Rep 50(1–2):1–78. https://doi.org/10.1016/j.mser.2005.07.001
11. Cui L et al (2018) Recent progress in friction stir welding tools used for steels. J Iron Steel Res Int 25(5):477–486. https://doi.org/10.1007/s42243-018-0066-7
12. Ferreira FB, Felice I, Brito I, Oliveira JP, Santos T (2023) A Review of Orbital Friction Stir Welding. Metals 13(6):1055. https://doi.org/10.3390/met13061055
13. Senthil SM, Bhuvanesh MK, Dennison MS (2022) A Contemporary Review on Friction Stir Welding of Circular Pipe Joints and the Influence of Fixtures on This Process. Adv Mater Sci Eng 2022:1–25. https://doi.org/10.1155/2022/1311292
14. Liu FC et al (2018) A review of friction stir welding of steels: Tool, material flow, microstructure, and properties. J Mater Sci Technol 34(1):39–57. https://doi.org/10.1016/j.jmst.2017.10.024
15. Venkatesh KM et al (2018) Review on friction stir welding of steels. Mater Today: Proc 5(5):13227–13235. https://doi.org/10.1016/j.matpr.2018.02.313
16. Youlia RP et al (2023) A review towards Friction Stir Welding technique: working principle and process parameters. Sinergi 27(3):289. https://doi.org/10.22441/sinergi.2023.3.001
17. Abbasi M, Abdollahzadeh A, Bagheri B et al (2021) Study on the effect of the welding environment on the dynamic recrystallization phenomenon and residual stresses during the friction stir welding process of aluminum alloy. Proc Inst Mech Eng Part L: J Mater Des Appl 235(8):1809–1826. https://doi.org/10.1177/14644207211025113
18. Bagheri B, Shamsipur A, Abdollahzadeh A et al (2023) Investigation of SiC Nanoparticle Size and Distribution Effects on Microstructure and Mechanical Properties of Al/SiC/Cu Composite during the FSSW Process: Experimental and Simulation. Met Mater Int 29:1095–1112. https://doi.org/10.1007/s12540-022-01284-8
19. Lammlein DH, Gibson BT, DeLapp DR, Cox C, Strauss AM, Cook GE (2012) The friction stir welding of small-diameter pipe: an experimental and numerical proof of concept for automation and manufacturing. Proc Inst Mech Eng Part B J Eng Manuf 226(3):383–398. https://doi.org/10.1177/0954405411402767
20. Abbasi M, Bagheri B, Abdollahzadeh A et al (2021) A different attempt to improve the formability of aluminum tailor welded blanks (TWB) produced by the FSW. Int J Mater Form 14:1189–1208. https://doi.org/10.1007/s12289-021-01632-w
21. Abdollahzadeh A, Bagheri B, Abbasi M et al (2021) A modified version of friction stir welding process of aluminum alloys: Analyzing the thermal treatment and wear behavior. Proc Inst Mech Eng Part L: J Mater Des Appl 10:2291–2309. https://doi.org/10.1177/14644207211023987
22. Bhardwaj N, Narayanan RG, Dixit US, Hashmi MSJ (2019) Recent developments in friction stir welding and resulting industrial practices. Adv Mater Proc Technol 5(3):461–496. https://doi.org/10.1080/2374068X.2019.1631065
23. Song KH, Kim WY, Nakata K (2012) Evaluation of microstructures and mechanical properties of friction stir welded lap joints of Inconel 600/SS 400. Mater Des 35:126–132. https://doi.org/10.1016/j.matdes.2011.09.054
24. Rodriguez J, Ramirez AJ (2015) Microstructural characterisation of friction stir welding joints of mild steel to Ni-based alloy 625. Mater Charact 110:126–135. https://doi.org/10.1016/j.matchar.2015.10.023
25. De Lima Lessa CR et al (2020) Two-Pass Friction Stir Welding of Cladded API X65. Procedia Manuf 47:1010–1015. https://doi.org/10.1016/j.promfg.2020.04.311
26. Landell RM, De Lima Lessa CR, Bergmann L, Dos Santos JF, Kwietniewski CEF, Klusemann B (2021) Investigation of friction stir welding process applied to ASTM 572 steel plate cladded with Inconel®625. Weld World 65(3):393–403. https://doi.org/10.1007/s40194-020-01007-w
27. Bossle EP et al (2023) Friction Stir Lap Welding of Inconel 625 and a High Strength Steel. Metals 13(1):146. https://doi.org/10.3390/met13010146
28. Amavisca CV et al (2023) Feasibility of orbital friction stir welding on clad pipes of API X65 steel and Inconel 625. Sci Rep 13(1):10669. https://doi.org/10.1038/s41598-023-37913-4
29. ISO 4136 (2022) Destructive tests on welds in metallic materials - Transverse tensile test. 2022(E)
30. API Specification 5L, Line pipe (2018) 46th edn
31. DNV GL (2018) Rules for Classification of Ships, Part 2. Materials and welding, Chapter 2. Metallic materials. DNVGL-RU-SHIPS P.2 Ch.2: 2018
32. ASTM B705-17 (2017) Standard specification for nickel-chromium-molybdenum-niobium alloy, nickel-chromium-molybdenum-silicon alloy, and nickel-iron-chromium-molybdenum-copper alloy welded pipe, ASTM International
33. Aydin H, Nelson TW (2013) Microstructure and mechanical properties of hard zone in friction stir welded X80 pipeline steel relative to different heat input. Mater Sci Eng A 586:313–322. https://doi.org/10.1016/j.msea.2013.07.090
34. Wei L, Nelson TW (2012) Influence of heat input on post weld microstructure and mechanical properties of friction stir welded HSLA-65 steel. Mater Sci Eng A 556:51–59. https://doi.org/10.1016/j.msea.2012.06.057
35. Fairchild D et al (2009) Research concerning the friction stir welding of linepipe steels. In: ASM Trends in Welding Research: Proceedings of the 8th International Conference, p 371–380
36. Mohammdijoo M et al (2018) Characterization of martensite-austenite constituents and micro-hardness in intercritical reheated and coarse-grained heat affected zones of API X70 HSLA steel. Mater Charact 142:321–331. https://doi.org/10.1016/j.matchar.2018.05.057
37. Buzzatti DT et al (2022) Effect of heat input and heat treatment on the microstructure and toughness of pipeline girth friction welded API 5L X65 steel. Mater Sci Eng A 833:1425888. https://doi.org/10.1016/j.msea.2021.142588
38. Dialami N, Cervera M, Chiumenti M (2020) Defect formation and material flow in Friction Stir Welding. Eur J Mech A-Solid 80:103912. https://doi.org/10.1016/j.euromechsol.2019.103912
39. Bagheri B, Alizadeh M, Mirsalehi SE et al (2022) Nanoparticles Addition in AA2024 Aluminum/Pure Copper Plate: FSSW

Approach, Microstructure Evolution, Texture Study, and Mechanical Properties. JOM 74:4420–4433. https://doi.org/10.1007/s11837-022-05481-z
40. Abdollahzadeh A, Bagheri B, Shamsipur A (2023) Development of Al/Cu/SiC bimetallic nano-composite by friction stir spot welding. Mater Manuf Process 38(11):1416–1425. https://doi.org/10.1080/10426914.2022.2157435
41. Hanke S, Lemos GVB, Bergmann L, Martinazzi D, Dos Santos JF, Strohaecker TR (2017) Degradation mechanisms of pcBN tool material during Friction Stir Welding of Ni-base alloy 625. Wear 376–377:403–408. https://doi.org/10.1016/j.wear.2017.01.070
42. Harris TK, Brookes EJ, Taylor CJ (2004) The effect of temperature on the hardness of polycrystalline cubic boron nitride cutting tool materials. Int J Refract Met Hard Mater 22(2–3):105–110. https://doi.org/10.1016/j.ijrmhm.2004.01.004
43. Thompson B, Babu SS (2010) Tool degradation characterization in the friction stir welding of hard metals. Weld J 89:256-s-261-s. https://app.aws.org/wj/supplement/WJ122010_256.pdf. Accessed Mar 2024
44. Mina EM, da Silva YC, Dille J, Silva CC (2016) Effect of dilution on Microsegregation in AWS ER NiCrMo-14 Alloy Welding Claddings. Metall Mater Trans A 47A. https://doi.org/10.1007/s11661-016-3786-y
45. David SA, Siefert JA, DuPont JN, Shingledecker JP (2015) Weldability and weld performance of candidate nickel base superalloys for advanced ultrasupercritical fossil power plants part I: fundamentals. Sci Technol Weld Join 20(7):532–552. https://doi.org/10.1179/1362171815Y.0000000035
46. Wei L, Nelson TW (2012) Influence of heat input on post weld microstructure and mechanical properties of friction stir welded HSLA-65 steel. Mater Sci Eng: A 556:51–59. https://doi.org/10.1016/j.msea.2012.06.057
47. Feng Z, Steel R, Packer S, David SA (2009) Friction Stir Welding of API Garde 65 Steel Pipes. In*:* Materials and Fabrication, Parts A and B, Prague, Czech Republic. Vol. 6, ASMEDC, p 775–779. https://doi.org/10.1115/PVP2009-77248
48. Ayer R, Jin HW, Mueller RR, Ling S, Ford S (2005) Interface structure in a Fe–Ni friction stir welded joint. Scr Mater 53(12):1383–1387. https://doi.org/10.1016/j.scriptamat.2005.08.042
49. Murr LE (2010) A Review of FSW Research on Dissimilar Metal and Alloy Systems. J Mater Eng Perform 19(8):1071–1089. https://doi.org/10.1007/s11665-010-9598-0
50. Lemos GVB, Hanke S, Dos Santos JF, Bergmann L, Reguly A, Strohaecker TR (2017) Progress in friction stir welding of Ni alloys. Sci Technol Weld Join 22(8):643–657. https://doi.org/10.1080/13621718.2017.1288953
51. Song KH, Nakata K (2010) Effect of precipitation on post-heat-treated Inconel 625 alloy after friction stir welding. Mater Des 31:2942–2947. https://doi.org/10.1016/j.matdes.2009.12.020
52. Cho H-H et al (2012) Microstructural evolution in friction stir welding of high-strength linepipe steel. Mater Des 34:258–267. https://doi.org/10.1016/j.matdes.2011.08.010
53. Barnes SJ et al (2012) Friction Stir Welding in HSLA-65 Steel: Part I. Influence of Weld Speed and Tool Material on Microstructural Development. Metall Mater Trans A 43(7):2342–2355. https://doi.org/10.1007/s11661-012-1110-z
54. Zhang ZH, Li WY, Feng Y, Li JL, Chao YJ (2015) Global anisotropic response of friction stir welded 2024 aluminum sheets. Acta Mater 92:117–125. https://doi.org/10.1016/j.actamat.2015.03.054
55. Su Y et al (2021) Comparing the local-global deformation mechanism in different friction stir welding sequences of Ti-4Al-0.005B titanium alloy T-joints. Mater Sci Eng A 823:141698. https://doi.org/10.1016/j.msea.2021.141698
56. Balan KP (2018) Metallurgical failure analysis: techniques and case studies. Elsevier. https://doi.org/10.1016/B978-0-12-814336-0.00008-1
57. Bagheri B, Alizadeh M, Mirsalehi SE et al (2022) The effect of rotational speed and dwell time on Al/SiC/Cu composite made by friction stir spot welding. Weld World 66:2333–2350. https://doi.org/10.1007/s40194-022-01376-4
58. Shrestha SL et al (2014) An automated method of quantifying ferrite microstructures using electron backscatter diffraction (EBSD) data. Ultramic 137:40–47. https://doi.org/10.1016/j.ultramic.2013.11.003